Quasi-3D harnessing of visible light in emissive III-V on Si microstructures: Application to multiple-quantum-well color conversion layers

Amade Ndiaye, Ahlem Ghazouani, Romain Sommer, Elisa Vermande, Christine Di Nardo, Christian Seassal, Emmanuel Drouard, Christophe Jany, Badhise Ben Bakir

Micro and Nanostructures 185 (2024) 207721

Contents lists available at ScienceDirect

Micro and Nanostructures

journal homepage: www.journals.elsevier.com/micro-and-nanostructures

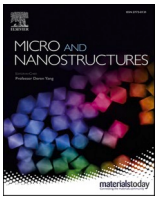

Quasi-3D harnessing of visible light in emissive III-V on Si microstructures: Application to multiple-quantum-well color conversion layers

Amade Ndiaye [a,**], Ahlem Ghazouani [a], Romain Sommer [a], Elisa Vermande [a], Christine Di Nardo [a], Christian Seassal [b], Emmanuel Drouard [b], Christophe Jany [a], Badhise Ben Bakir [a,*]

[a] Univ. Grenoble Alpes, CEA, LETI, F-38000, Grenoble, France
[b] Univ. Lyon, Institut des Nanotechnologies de Lyon-INL, UMR CNRS 5270, CNRS, Ecole Centrale de Lyon, Ecully, F-69134, France

ARTICLE INFO

Keywords:
Light extraction
Bloch modes
Color conversion
MQW
FDTD
microLED (μLED)

ABSTRACT

We report on the design, fabrication, and characterization of the first photonic crystal (PhC)-based red multiple-quantum-well (MQW) color converters fully optimized for augmented reality (AR) microdisplays through a quasi-3D light harnessing principle. This principle leverages an aluminum (Al) bottom reflector and a silicon dioxide (SiO_2) gap to harness the bottom-emitted light, along with copper (Cu) lateral mirrors and a silicon nitride (SiN) phase-matcher for Bloch-mode replication. These structures were designed using 3D-FDTD simulations. As a proof-of-principle, we fabricated corresponding devices that exhibit promising characteristics, including record light extraction efficiencies over 40 % for 4 μm pixels and directional emission patterns. Time-resolved photoluminescence (TRPL) analyses, along with a four-wave intensity model developed in this work, indicate that there is still room for improvement. We believe that the guidelines established in this study could pave the way for the use of MQW color converters in the next generation of very bright, high-resolution RGB microdisplays for AR glasses and beyond.

1. Introduction

MQW color conversion layers (CCL) have the potential to revolutionize augmented reality (AR) microdisplays by offering an alternative to state-of-the-art quantum dot (Q-dot) color converters, especially in situations where high luminance (due to photo-stability concerns) and high resolutions (requiring compact integration schemes) are required, such as in the case of InGaP/AlGaInP MQW for blue-to-red color conversion [1–3]. However, their implementation still faces several challenges. The first challenge is related to their low light extraction efficiency (LEE) inherent to the high refractive index contrast between III-V materials and the outside medium (air or low index material). Indeed, AlGaInP-based materials have refractive indices over three in the visible spectral range, so most of the emitted red light will couple to the available guided modes inside the so-formed membrane and drastically limit their maximum reachable conversion efficiencies to ~3 % [1]. Recent evaluations have indicated that for CCL to achieve the targeted

* Corresponding author.
** Corresponding author.
E-mail addresses: amade.ndiaye@ams-osram.com (A. Ndiaye), badhise.ben-bakir@cea.fr (B. Ben Bakir).

https://doi.org/10.1016/j.micrna.2023.207721
Received 30 June 2023; Received in revised form 8 November 2023; Accepted 17 November 2023
Available online 21 November 2023

luminance in AR microdisplays, efficiency values between 40 and 50 % are required [2]. Therefore, addressing these light extraction issues is crucial, and there is still a significant gap to overcome.

A schematic side view of a possible integration strategy of those MQW color converters on a blue μ-LED array is displayed in Fig. 1 [3]. A GaN-based blue μ-LED array is used to pump blue-to-green and blue-to-red MQW CCL, with a specific focus on the blue-to-red color conversion in this work. In addition to addressing light extraction issues, there are other application-driven requirements that need to be considered.

Firstly, resolution is a key element in the product development for AR microdisplays. Indeed, in such applications, pixel lateral sizes denoted L_{pixel} can be less than 5 μm. This means that not only should a significant part of the emitted light be extracted, but also the extraction length L_{ext}, which represents the lateral extent needed to extract the guided light, needs to be shorter than L_{pixel}. Furthermore, since these applications include systems with limited numerical apertures (NA), the CCL should also exhibit highly directional emission to efficiently couple with optical systems, which is not met yet due to the Lambertian-like farfield emission patterns of AlGaInP MQW CCL [4]. Lastly, the technological integration of red CCL onto on-silicon blue μ-LED arrays in 200 mm cleanroom facilities can be challenging, as the epitaxial structures are initially on 3-inch diameter GaAs substrates and need to be efficiently transferred onto the receiving substrates as well as pixelated [1]. All the aforementioned issues are summarized in Table 1 and must be addressed to establish this strategy as a credible alternative to Q-dots in AR microdisplays.

Photonic-crystals (PhCs), which are periodic dielectric modulations at wavelength-scale, have been widely used to achieve high LEE in high refractive-index material systems [5–7]. Due to the coherent nature of their diffraction process, they also have the unique ability to outcouple guided modes and provide superior control over farfield emission patterns all at once [5]. In addition, when properly designed and combined with thin-film devices, PhCs can exhibit a strong interaction with guided Bloch-modes, leading to short extraction lengths [6]. In recent studies, our group reported on the first PhC-based AlGaInP/InGaP MQW CCL fully optimized for blue-to-red color conversion in AR microdisplays. The opto-geometrical parameters of the PhC were tuned to achieve significant LEE enhancement factors and directional emission [2,3].

However, in those previous investigations, a comprehensive assessment of the actual efficiencies of the color converters in real-life RGB microdisplays could not be conducted due to various reasons. Firstly, the color converters were on transparent substrates, resulting in a significant part of the emitted light being coupled to substrate modes. Secondly, the MQW color converters were unpixelated, so that the impact of the lateral mirrors used to reduce pixel optical crosstalk in RGB microdisplays on the overall conversion efficiency was not accounted for.

In real-life like RGB microdisplays, the MQW color converters would be bonded on the blue pump, forming a membrane with a gap mimicking the blue μLED and the bonding layers, along with a bottom reflector simulating the p-side electrical injection metal of the pumping LED. In addition, as mentioned earlier, the MQW color converters are pixelated and surrounded by lateral mirrors to avoid optical crosstalk in-between the pixels [3]. This configuration is depicted in Fig. 2. It is therefore of paramount importance to investigate the performances of these red MQW color converters under real-life like conditions, including back- and lateral-mirrors, a gap between the converter and the bottom reflector, and other factors, which we tackle in this paper.

In this work, we then report on the design, fabrication and characterization of the first PhC-based InGaP/AlGaInP red MQW color converters fully optimized for AR microdisplays through a quasi-3D light harnessing principle. This principle takes benefit from an Al bottom reflector following a SiO_2 gap (to harness the bottom emitted light) as well as Cu lateral mirrors combined with a SiN phase-matcher (for Bloch-mode replication), all designed using 3D-FDTD simulations. Section 2 outlines the design principles of the devices, while their integration & fabrication in 8-inch cleanroom facilities are detailed in Section 3. The results are analyzed and discussed in Section 4, presenting record efficiencies and providing guidelines for further improvement.

2. Design principles

In this section, we employ 3D-FDTD simulations to define the design principles for using photonic crystals (PhCs) along with a quasi-3D light harnessing technique to achieve the targeted performances for red AlGaInP/InGaP MQW color converters in AR microdisplays. The red color converters are based on the AlGaInP epitaxial stack reported here [1].

As mentioned above, we use PhCs to enhance μLED LEE. The PhCs consist of square lattice of nanopillars with a lattice period of a = 400 nm, ensuring that each guided mode supported by our CCL can be prone to diffraction into air, a lateral extent of 5 periods (for

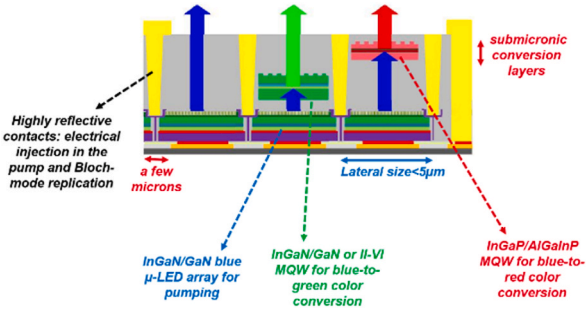

Fig. 1. Schematic side view of a possible integration strategy for monolithic RGB emission using MQW color converters [3].

Table 1
From display requirements to challenges for blue-to-red MQW color converters.

	Luminance	Resolution	Compactness	Integration technology
Pixels for AR microdisplays	Between 10^5 and 10^6 cd/m^2	L_{pixel}<5 μm	Avoid additional external optics	Feasibility
Challenges to overcome for AlGaInP/InGaP CCL	LEE between 40 and 50 %	L_{ext}< 5 μm	Directional emission through control of the emission pattern	Transfer of epilayers + pixelization

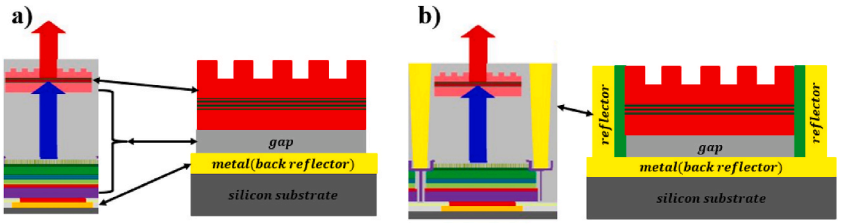

Fig. 2. a) Harnessing the bottom emitted light in MQW CCL with a back-reflector. b) Virtual extension of the pixel lateral sizes using the lateral mirrors. The gap mimics all the layers embedded between the CCL and the electrical contact, while the back-reflector represents the said contact. Lateral mirrors, on the other hand, enable the optical isolation of the pixels from each other and allow the non-extracted photons after the first pass in the grating to be reflected, providing additional chances to escape.

computing time issue), an etch depth of about the third of the total stack thickness and an air-filling factor of 50 % to achieve high coupling strengths between the guided Bloch-modes and the air-radiated modes. For a more detailed discussion on the choice of the PhCs parameters, we refer the reader to Ref. [1].

We perform incoherent 3D-FDTD simulations in a pulsed regime to calculate LEE and farfield patterns [7]. The excitation spectrum is Gaussian-shaped with a center wavelength at 640 nm and a FWHM of 20 nm corresponding to the photoluminescence (PL) signals of our epitaxial stack. The MQW region is represented by a single source plane of 50 transverse electric (TE)-polarized dipoles in the middle of the CCL.

We use Al as a bottom reflector to mimic the electrical contact at the bottom of the blue μ-LEDs in the final integration strategy (see Fig. 1) [8]. In addition, we opted for Cu lateral mirrors due to their higher reflectivity values in the red spectral range before which we interleaved a SiN passivation layer on the sidewall surface, between the MQW CCL and the Cu mirrors to limit internal quantum efficiency (IQE) decrease for pixels with short lateral sizes [9].

2.1. Phase-matching layer

In this subsection, we aim at discussing the advantages of implementing lateral Cu mirrors and SiN passivation layer to improve the LEE of MQW color converters.

As highlighted above, when photons pass through pixels with short lateral sizes (shorter than the extraction lengths), they are not completely extracted by the grating due to the low number of diffractive elements. In such case, the lateral mirrors can reflect the non-extracted photons and provide other opportunities for their escape toward free space. This principle can be referred to as Bloch-mode replication (BMR). In the ideal scenario, the incoming and reflected photons should have identical amplitude and phase which requires the lateral-mirror reflectance to be as high as possible in the red spectral range and the reflection phase-shift to be matched.

The SiN passivation layer will act as a phase matcher (PM) to overcome this latter issue. For this study, the MQW CCL lie on a transparent substrate (to decouple the effects of back- and lateral-mirrors) and is surrounded by Cu lateral mirrors. To determine the optimal values of the PM thickness, we performed 3D-FDTD simulations on the devices described in Fig. 3 a).

Fig. 3 b) reports on LEE on the top side of the device as a function of the optical thickness of the SiN PM. We observe that in the near-field regime (low optical thicknesses) LEE has intricate variations but overall increases as the PM optical thickness increases. It then reaches a first maximum of ~24 % for $n_{PM}d_{PM}/\lambda = 0.75$ where near-field effects do not seem to occur anymore, and reflection phase-shift appears to be matched. It subsequently continues to oscillate due to interference processes with a $\lambda/2$ periodicity and decreasing amplitudes.

These variations can be easily understood by considering the case of an ideal reflector. If we note φ_{metal} the phase-shift induced by the lateral mirror and φ_{PM} the additional phase stemming from the propagation in the PM, we can write that for a perfect BMR the following condition needs to be satisfied:

$$\varphi_{metal} + 2\varphi_{PM} = 2p\pi, \text{with } p \text{ an integer and} \varphi_{PM} = 2\pi\frac{\widetilde{n}_{PM}d_{PM}}{\lambda} \quad (1)$$

here d_{PM} is the thickness of the PM and $\widetilde{n}_{PM}$ is a mean effective index, considering the multimode nature of the structure. For an ideal mirror ($\varphi_{metal} = \pi$), the previous condition implies that the maxima of LEE are reached for:

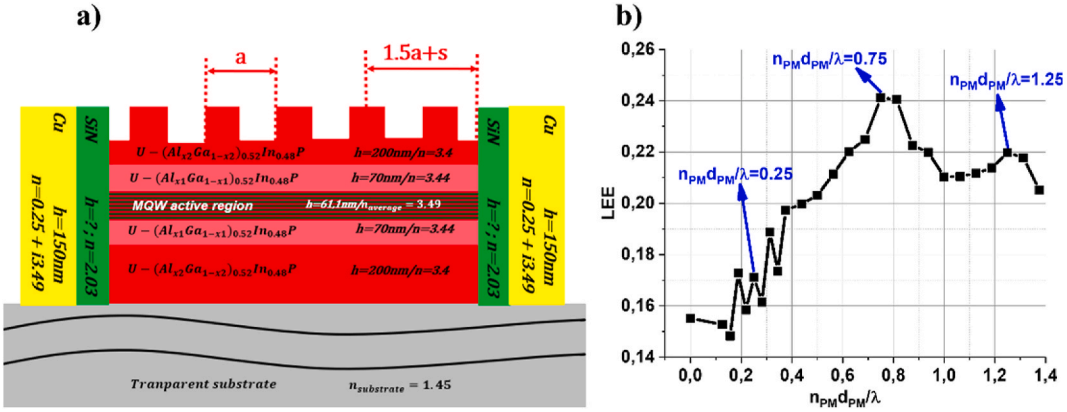

Fig. 3. 3D-FDTD simulation for determining the phase-matcher (PM) thickness. a) Red MQW color-converter on a transparent substrate surrounded by Cu-based lateral mirrors and SiN PM to compensate for the reflection phase-shift. The parameter *s* represents a technological oversizing ($s > 0$) or an under-sizing ($s < 0$) of the mesa and *a* is the lattice period. b) Light extraction efficiency (top side) as a function of the PM optical thickness.

$$\frac{\widetilde{n}_{PM}d_{PM}}{\lambda} = 0.25\times(2p-1) with\ p\ a\ non-zero\ integer \quad (2)$$

In Fig. 3 b), the first maximum at ~0.25 is not reached due to near-field effects, however the second (0.75, p = 2) and third (1.25, p = 3) ones appear located closely to the positions predicted in the former equation. As the lateral thickness increases to very high values, the amplitudes of the maximum values decrease suggesting a reduced interaction between the guided light and the lateral mirrors. It is worth noting that due to the multimode nature of the MQW CCL (many different effective indices) the phase-condition in Eq. (1) is not ideal, which is why the oscillations after the near-field regime are not clear-cut.

Either way, the optimal value for the optical thickness of the PM (in the case of Cu lateral mirrors) is ~0.75λ, which would correspond to a SiN thickness of 240 nm. This very thick layer can be technologically tricky[1] to deposit on the sidewall surface of the MQW CCL. Consequently, as we will see in Section 3, we only deposit a ~70-nm-thick SiN layer (~0.2λ) on the sidewalls and the remaining optical thickness (~0.55λ) will be compensated by slightly increasing the mesa size. It's worth noting that one alternative to the increase of the mesa size could be to use a phase-matcher with a higher refractive index than SiN in the red spectral range, e.g. TiO_2. The maximum LEE on the top side of the structure is ~24 % because part of the emitted light (~50 %[2]) is extracted inside the transparent substrate and another one is lost due to absorption in the lateral mirrors. An additional study of the robustness of the design (not shown here) has also been performed using 3D-FDTD simulations to evaluate the impact of a technological oversizing or under-sizing of the mesa ($s > 0$ or $s < 0$, see Fig. 3 a)) due to a misalignment between the mesa and grating levels. It has been found that as long as *s* is kept under 30 nm LEE is only slightly impacted.

2.2. Gap between the MQW CCL and the bottom reflector

As previously discussed, when the MQW color converters lie on a transparent substrate, a large part of the emitted light is lost in the substrate. In real-life RGB microdisplays (see Figs. 1 and 2), the MQW CCL are bonded on blue μ-LED arrays with intermediate oxide bonding layers in-between. For the sake of demonstration, a SiO_2 gap layer is interleaved between the MQW CCL and the Al back reflector in the fabricated devices to mimic the blue μ-LEDs. The SiN PM layer thickness is set to the optimal value found in the previous subsection. We conduct 3D-FDTD simulations to determine the optical thickness of the SiO_2 gap necessary to harness the bottom emitted light.

The simulated structure (see Fig. 4) is the same as the one before, albeit on an Al back reflector and with a SiO_2 gap in-between. Fig. 4 b) displays LEE on the top side of the device as a function of the SiO_2 gap optical thickness. Similarly to before, LEE increases in the near-field regime until it reaches its first maximum of ~45 % at $n_{gap}d_{gap}/\lambda = 0.63$. It then continues to oscillate due to interference processes with also a λ/2 periodicity (unity round-trip condition) and decreasing amplitudes. Since dipolar emission is omnidirectional, the oscillations after the near-field regime are not as well-defined as they would be for a plane-wave impinging on the back reflector at normal incidence.

During the fabrication, we will thus choose a 350-nm-thick SiO_2 gap, which is close to the aforementioned first maximum. At this optimal condition, directional emission can also be reached as shown in the calculated azimuthal radiation patterns in Fig. 4 c), where most of the emitted light is concentrated into a ±30° cone.

[1] To obtain 240-nm-thick SiN layer on the sidewall of the MQW CCL, one needs to deposit more than ~350 nm on the top side. Because of selectivity issues between the photoresist and SiN, this could be detrimental later in the etching process for the SiN-layer removal.

[2] We evaluated the bottom emitted light by placing a monitor inside the transparent substrate during the FDTD simulations.

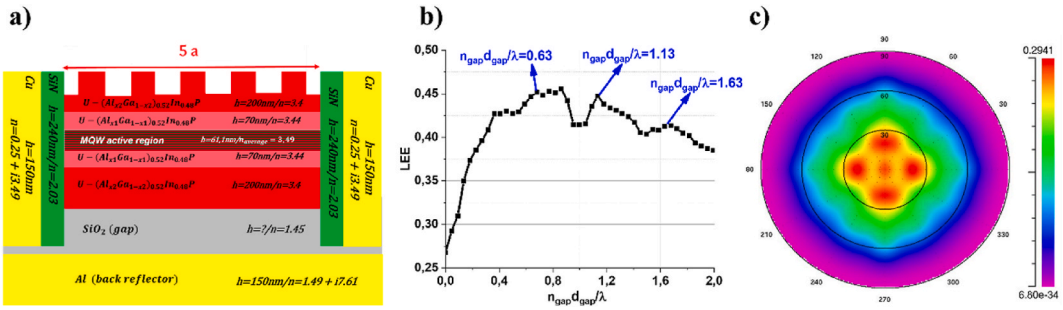

Fig. 4. 3D-FDTD simulation results to determine the optimal gap (SiO_2) thickness. a) Cross section of the final devices comprising MQW CCL surrounded by Cu lateral mirrors with a SiN phase matcher as well as Al back reflector with a SiO_2 gap. b) Light extraction efficiency as a function of the gap optical thickness. c) Azimuthal farfield radiation patterns of devices with $n_{gap}d_{gap}/\lambda = 0.63$.

2.3. Conclusion on the design principles and device architecture

It appears that one can effectively leverage the electromagnetic environment of the MQW color converters to increase their LEE in two ways, while maintaining directional emission. FDTD simulations have initially helped us demonstrate that by introducing a 350-nm-thick SiO_2 gap between an Al back reflector and the MQW CCL, one could harness a significant part of the bottom emitted light to promote top emission. Moreover, when the reflection phase-shift induced by the penetration inside the lateral mirrors is matched, Bloch-mode replication could be a promising way to increase the LEE further. This latter requires an additional phase matching medium with an optical thickness of ~0.75λ in the case of Cu lateral mirrors, which can be performed with a simultaneous adaptation of the SiN passivation layer thickness and the lateral size of the mesa structure.

As a proof-of-principle demonstration of this quasi-3D light harnessing strategy, we fabricated in the following section MQW color converters in a pixel geometry embedding an Al bottom reflector, SiO_2 gap, Cu lateral mirrors as well as SiN phase matcher based on previous considerations to assess the expected performances of those MQW color converters in real-life RGB microdisplays.

3. Device fabrication

In this section, we describe the fabrication process of the pixelated MQW color converters with back- and lateral-mirrors described in Fig. 4 a). The starting AlGaInP epitaxial structure is depicted in Table 2. It is an epi-layer grown lattice matched on a 3-inch diameter GaAs substrate. Its measured emission peak wavelength and the full width at half-maximum (FWHM) are ~640 nm and ~20 nm, respectively. Layers 0, 1, 2 and 3 will be removed in the integration process.

The III-V on Si integration as well as the device fabrication was achieved in the CEA-LETI's 8-inch ICs/MEMS cleanroom facilities.

It is worth noting that the complete and functional integration flow, which is shown in Fig. 5, is a result of extensive process development on most of the technological steps.

The first step is to transfer the red epilayer onto the receiving substrates, which are 200 mm Si substrates metallized with Ti bonding layers deposited by PVD and followed by CMP to enable planarization and surface activation. The 350-nm-thick SiO_2 (gap to mimic the blue μLED and the bonding layers in the final integration scheme) is deposited on the epitaxial structure (layer 9), preceded by a 10-nm-thick ALD alumina intermediate layer to favor optimal adherence. Next, a PVD-deposited 150 nm-thick Al on top of the SiO_2 gap acts as a back reflector. A 5 nm-thick PVD-Ti layer was interleaved between the SiO_2 and the back reflector for adherence purposes and then followed by an additional Ti bonding layer. The two surfaces are cleaned and oxygen plasma ensued to activate them. We then achieve the bonding by putting the wafers in contact at room temperature, followed by a 300 °C annealing for 90 min to reinforce the bonding strength.

Scanning acoustic microscope (SAM) images of the bonded red MQW CCL before and after annealing are displayed in Fig. 6 a) and

Table 2
III-V epitaxial growth layer structure and characteristics.

Layer	Material	Thickness	Refractive indices at λ = 640 nm
0: Substrate	GaAs	625 μm	
1: Buffer layer	U-GaAs	200 nm	
2: Etch-stop layer	U-InGaP	300 nm	
3: Sacrificial layer	U-GaAs	50 nm	
4: Cladding	$U\text{-}(Al_{x2}Ga_{1-x2})_{0.52}In_{0.48}P$	200 nm	n = 3.4
5: MQW barrier	$U\text{-}(Al_{x1}Ga_{1-x1})_{0.52}In_{0.48}P$	70 nm	n = 3.44
6: MQW region	$4\times U\text{-}In_yGa_{1-y}P/5\times U\text{-}(Al_{x1}Ga_{1-x1})_{0.52}In_{0.48}P$	4.4 nm/8.7 nm	$n_{average} = 3.49$
7: MQW barrier	$U\text{-}(Al_{x1}Ga_{1-x1})_{0.52}In_{0.48}P$	70 nm	n = 3.44
8: Cladding	$U\text{-}(Al_{x2}Ga_{1-x2})_{0.52}In_{0.48}P$	200 nm	n = 3.4
9: Bonding interface	U-GaAs	20 nm	

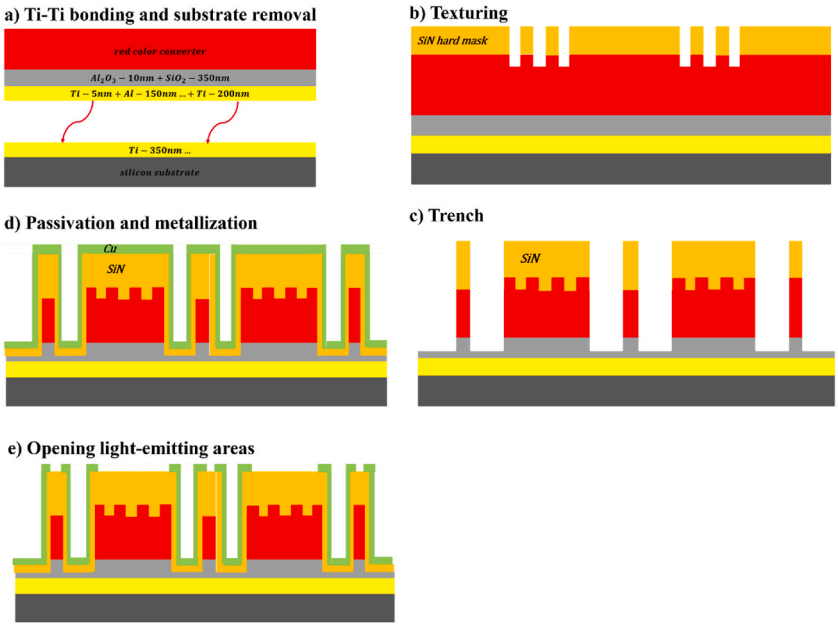

Fig. 5. Complete process flow of the devices fabricated in this work showing the 3-etching-level technology after bonding (texturing for photonic-crystal fabrication, Trench for pixelization and Open for removing the metal on top of the light-emitting areas).

Fig. 6 b) showing that it helps reach high bonding yield (>95 %).

Thereupon, the GaAs substrate and the sacrificial layers are removed by highly selective wet etching techniques. Fig. 6 c) reports on the bonded epilayer after substrate and sacrificial layer removal on 200 mm metallized silicon substrate. The remaining thickness of the red MQW CCL is around 600 nm.

After the bonding and substrate removal, the next steps of the process are achieved throughout a 3-etching-level lithography (see Fig. 5): texturing level for photonic-crystal (PhC) fabrication, trench level for mesa definition and open level after metallization to uncover light-emitting areas.

The texturing level was achieved using e-beam lithography and a top-down pattern-transfer approach through a SiN hard mask. 1D as well as square and hexagonal lattices of air holes and pillars (later referred to as SLAH for square lattice of air holes, SLNP for square lattice of nanopillars, TLAH for triangular lattice of air holes and TLNP for triangular lattice of nanopillars) have been fabricated with various opto-geometrical parameters. For each one, lattice periods have been varied from 400 nm to 700 nm with a step of 50 nm. In addition, for each lattice period, PhC structures with different lateral extents have been fabricated for this study: 3, 5, 10, 25 and 40 periods. The etch depth and air-filling factor have been set to the optimal values found in the previous section (~180 nm and ~50 %, respectively). SEM images of some of the fabricated structures are presented in Fig. 7.

We can note the presence of SiN blisters, which are some defects resulting from the non-conformity of the low-stress PECVD-SiN on GaAs.

For the trench level, we opted for 248 nm Deep UV lithography followed by RIE etching, since the critical dimension (CD) of the trenches is 1 μm. The etching process is similar to the one used during PhC-pattern definition, albeit with a thicker SiN hard mask[3] (250 nm). In Fig. 8, we show a focused ion beam (FIB) image of the 1D lattice during the etching process for the trench level right after the hard-mask opening.

Subsequently, the structure is etched all the way through the remaining 600-nm-thick red epilayer with a stop-etch inside the SiO_2, which has been confirmed by additional energy dispersive X-ray (EDX) analyses (not shown here). Top-view SEM images of some of the devices after the trench etching levels are shown in Fig. 9. It is worth pointing out that during the UV lithography, the overlay measurements showed that the misalignment between the texturing and trench levels was kept under 10 nm (3-sigma measurements over thousands of devices), which is of paramount interest for phase matching during BMR as pointed out in Section 2. In addition, the trench symmetry follows the ones of the PhC lattice to ensure efficient Bloch-mode replication (hexagonal trenches for hexagonal lattices and square ones for square lattices).

Afterwards, the trenches were filled[4] by a 100-nm-thick PECVD-SiN passivation and phase-matching layer as well as 150-nm-thick PVD Cu lateral mirrors, preceded by 5 nm-thick PVD-Ti for adherence purposes. Following this metallization, we opened light-–emitting areas using UV lithography followed by ion-beam etching (IBE) for removing the Cu layer on top of the device.

[3] The AlGaInP: SiN etching selectivity is around 3:1 within our technological conditions.

[4] Following the trials made in our lab, around 70 % of the thickness deposited on top of the device will be found on the sidewalls.

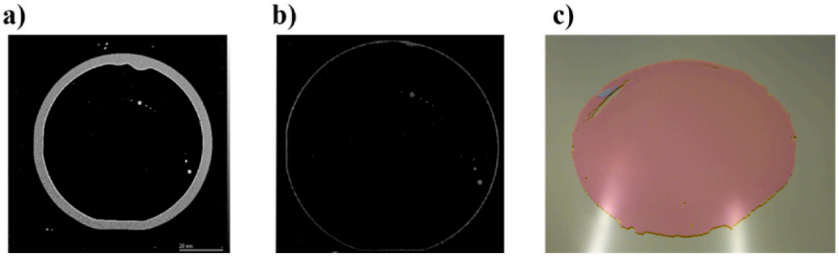

Fig. 6. Scanning acoustic microscopy (SAM) image of the bonded epilayer a) after it is put in contact with the silicon substrate and b) after a 300 °C annealing for 90 min to reinforce the bonding interface. c) Picture of the bonded epilayer (in red) after substrate removal.

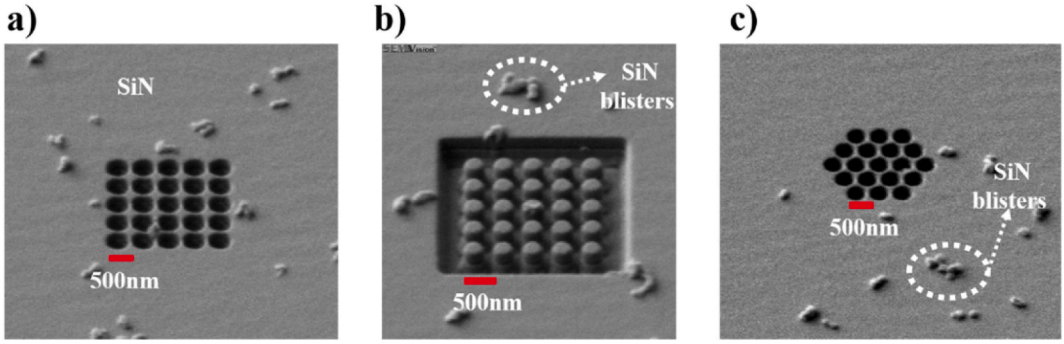

Fig. 7. Scanning electron microscopy (SEM) images of some of the fabricated devices after texturing. a) Square lattice of air holes and b) nano-pillars. c) Triangular lattice of air holes with a lattice period of a = 500 nm and a lateral extent of 5 periods. Due a non-conformity of the PECVD-SiN on GaAs, we notice the presence of SiN blisters mostly outside the emitting regions.

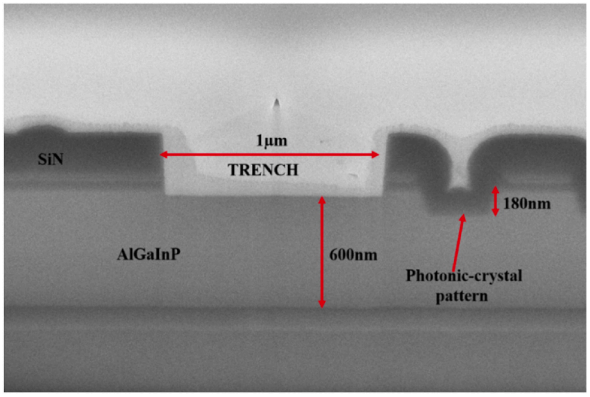

Fig. 8. Focused ion beam (FIB) image of the 1D lattice after hard mask etching for the trench level. The trench sidewalls are almost vertical while the ones of the photonic-crystal patterns are a bit tapered.

Fig. 10 shows SEM-EDX analyses performed on 1D lattices before and after metal etching, confirming that Cu has been completely etched on top of the light-emitting areas. The photoresist was then stripped, which concludes the process flow for these devices.

We eventually performed additional scanning transmission electron microscopy (STEM) analyses on some of the final devices to better visualize all the layers deposited during fabrication, particularly the SiN phase-matching layer and the lateral mirrors. Fig. 11 reports on high-resolution high-angle annular dark-field (HAADF) STEM images of a square lattice of air holes with a = 700 nm and a pixel lateral size of 3 periods, along with images with a zoom on the trenches. In addition, we conducted STEM-EDX analysis (see Fig. 12) to have a better insight into all the atoms and layers present in our final devices. The SiN phase-matching layer and Ti–Cu lateral mirrors, as well as the atoms composing the epitaxial structure (Al, Ga, As, In, P) have been well identified with thicknesses matching those we expected during fabrication from our design principles in Section 2.

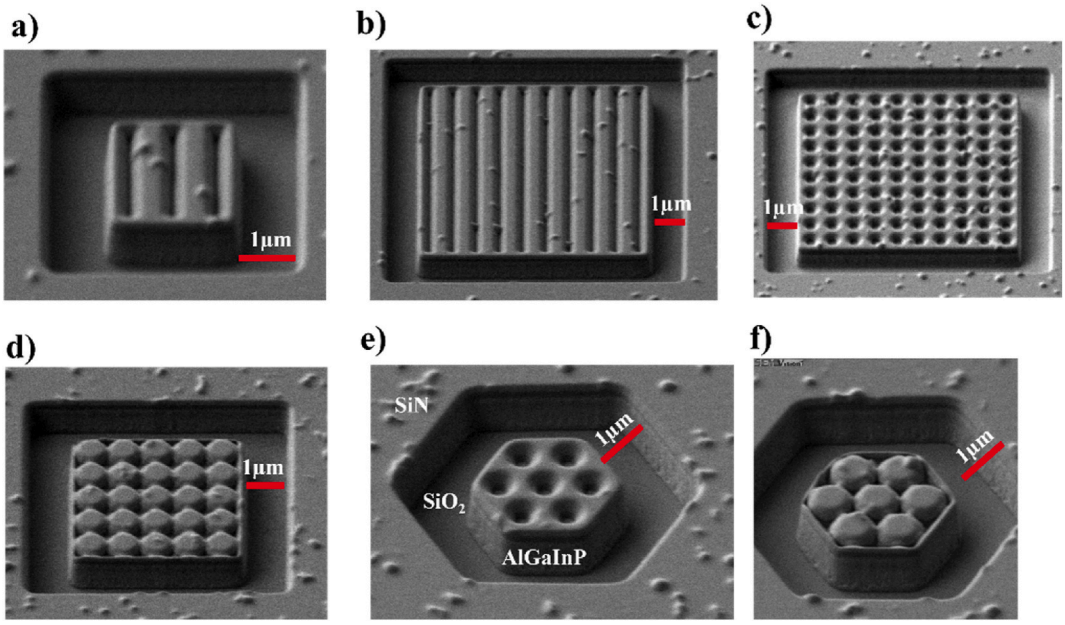

Fig. 9. Scanning electron microscopy (SEM) images of some of the fabricated devices after the trench etching level. a-b) 1D lattices with lateral extents of 3 and 10 periods, respectively. Square lattices of c) air holes and d) nanopillars. Hexagonal lattices of e) air holes and f) nanopillars.

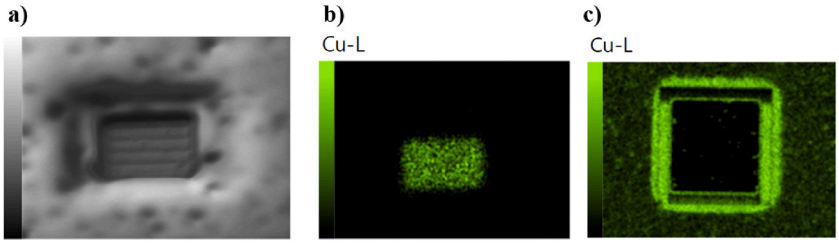

Fig. 10. a-b) SEM-EDX analysis and EDX analysis of 1D lattices before metal etching. c) EDX analysis after metal etching focusing on the presence of copper.

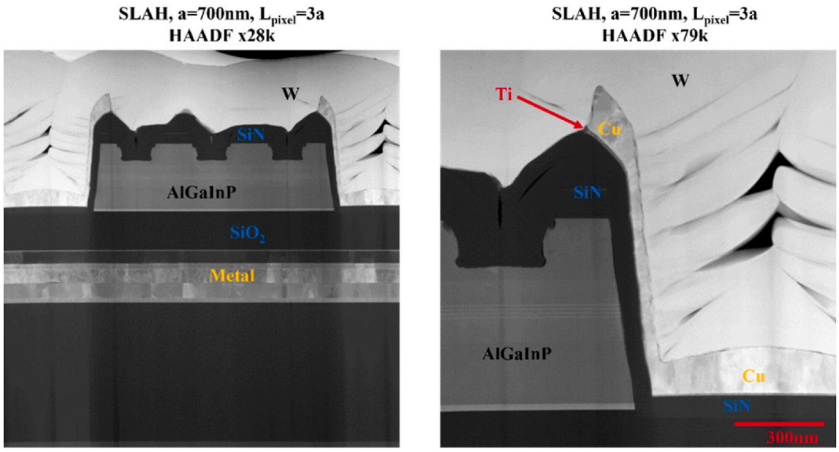

Fig. 11. HAADF-STEM images of the square lattice of air holes with a = 700 nm and L_{pixel} = 3a.

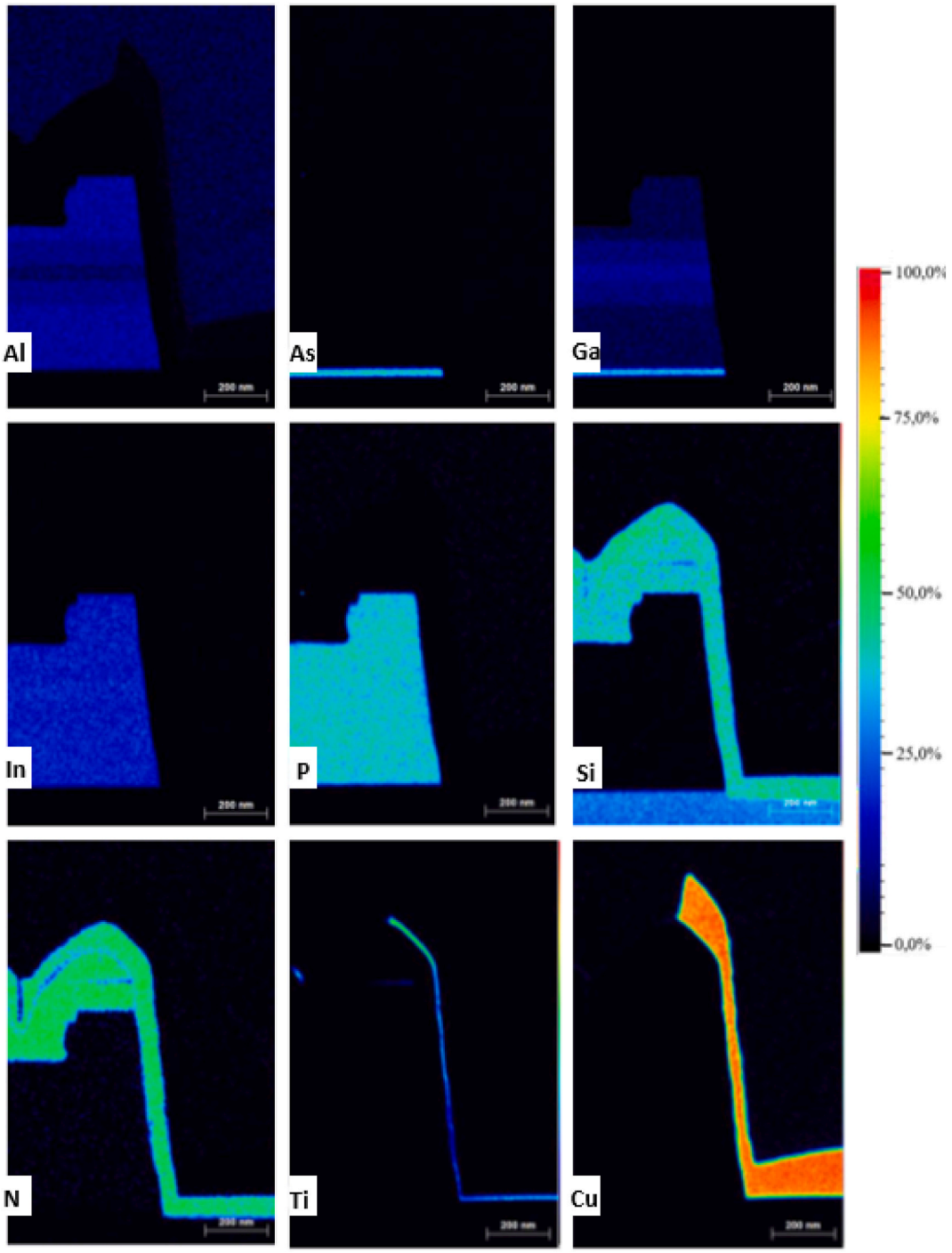

Fig. 12. STEM-EDX analyses of the trenches along with a quantification in terms of atomic percentage.

4. Results and discussion

4.1. Experimental evaluation of light extraction efficiency

To evaluate the experimental light extraction efficiency (LEE), we performed micro-photoluminescence (μ-PL) measurements with a LabRAM photoluminescence (PL) setup from HORIBA. A 405 nm laser line was focused on normal incidence by a microscope objective (MO) called excitation objective with a numerical aperture (NA) of 0.9 on the top side of the PhC structures. PL signals from

the samples were collected with the same excitation objective and dispersed by a spectrometer. The so-formed spectrum is then collected with a CCD camera. As in Ref. [1], we acquired PL spectra on the final devices (pixelated CCL with PhC, back- and lateral-mirrors) and on reference structures (unpixelated and unpatterned CCL). The ratio of the two previous spectra provide us with the PL enhancement factors for each device, which will be referred to as experimental LEE enhancement. From our 3D-FDTD simulations, we have evaluated that the LEE of the unpatterned and unpixelated MQW CCL on metallized-Si substrates amounts to ~12 %. By multiplying this reference value with the experimental LEE enhancement factors, we obtain an evaluation of the experimental LEE.

It is worth pointing out that our experimental LEE enhancement factors embed absorption enhancement, internal quantum efficiency (IQE) enhancement as well as LEE enhancement as already explained in Ref. [3]. The absorption efficiency is unchanged between the actual devices and the refences structures [1]. Therefore, our experimental LEE values are naturally underestimation of the real values of LEE since IQE decrease due to PhC and pixelization is embedded within, as explained in Ref. [1], but they still could give us a good insight into the performances reached.

Fig. 13 a) reports on the experimental LEE as a function of the pixel lateral size for the most performing fabricated device based on square lattice of nanopillars (SLNP) with a = 400 nm as well as back- and lateral mirrors.

We can observe that within the quasi-3D light harnessing principle the devices exhibit LEE values over ~40 %, which makes MQW color converters compatible with the initial requirements to reach high luminances for AR microdisplays (see Table 1). Next, we can also emphasize that those high LEE values are maintained provided the lateral extents of the pixels are kept over 2 μm, below which we notice a significant efficiency decrease from >40 % to ~20 %. This efficiency decrease could have two sources. First, when the pixel size is short (shorter than the extraction length), light undergoes many roundtrips inside the membrane and can be lost due to the lateral mirror reflectance (<100 %). On the other hand, since our experimental LEE also embeds IQE decrease, then this might also a role as large IQE decrease are observed in red emitting devices with shorter sizes due to non-radiative recombination [10]. A large-scale image of the blue-to-red photo-conversion process is shown in Fig. 13 b) where the overall intensity enhancement due to the PhC is clearly observed confirming this approach.

In the two following subsections, we will study separately these two phenomena and draw some guidelines regarding ways to circumvent them.

4.2. Understanding the impact of lateral-mirror losses: four-wave intensity model

As observed and pointed out in the experimental results, for pixel sizes shorter than the extraction length (inverse of the grating strength), light can be lost in the lateral mirrors. In this subsection, we wish to model that dependency of LEE on the coupling strength and the lateral-mirror reflectance to have a good insight into the interplay between light extraction and reflection as well as understand its role on Bloch-mode replication (BMR).

To do so, we herein propose a four-wave intensity model whose operating principle is depicted in Fig. 14. We start by assuming that the reflection phase-shift induced by the penetration depth inside the lateral mirrors is matched. In that framework, light emitted inside the CCL is either extracted outside by the grating, characterized by its coupling strength κ (mean coupling strength over all the guided Bloch-modes), or lost via lateral-mirror losses due to their reflectance values denoted R (<1). We note L_{pixel} the lateral extent of the pixel (also lateral size of the grating), I^z_{int} the intensity of the emitted light remaining inside the CCL after z half roundtrips, I^z_{out} the intensity of the portion of the emitted light extracted outside after z half roundtrips and I_0 the initial emitted light inside the membrane ($I^0_{int} = I_0$). The final light extraction efficiency at the end of this process is denoted LEE (on the top and bottom sides). For a more details about the coupling strengths, the extraction lengths and the other parameters, we refer the reader to Ref. [1].

Within that framework, the light intensity extracted outside after the first half roundtrip can be expressed using couple-mode-theory-derived model as in Ref. [1]:

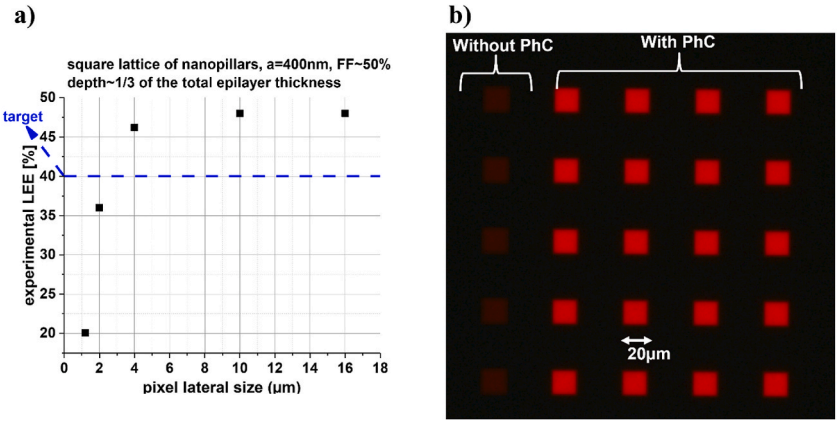

Fig. 13. a) Experimental LEE as a function of the pixel lateral sizes. b) Large-scale images of the blue-to-red photoconversion process on microled arrays.

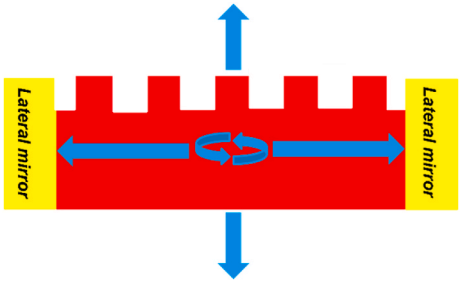

Fig. 14. Overview of the principle of the four-wave intensity model.

$$I_{out}{}^{1} = I_0 \, tanh^2(\kappa.L_{pixel}) \tag{3}$$

From that, we derive the remaining light intensity inside the membrane, which writes as[5]:

$$I_{int}{}^{1} = R(I_0 - I_{out}{}^{1}) = R(I_0 - I_0 \, tanh^2(\kappa.L_{pixel})) = R^1 \, I_0(1 - tanh^2(\kappa.L_{pixel}))^1 \tag{4}$$

We can thus more generally write that the remaining light intensity inside the cavity after z half roundtrips reads as:

$$I_{int}{}^{z} = R(I_0 - I_0 \, tanh^2(\kappa.L_{pixel})) = R^z \, I_0(1 - tanh^2(\kappa.L_{pixel}))^z \tag{5}$$

To determine LEE, we need to evaluate I_{out}^{∞} which is the total light intensity extracted outside at the end of the process. Using the previous equations, we can write:

$$I_{out}{}^{z+1} = I_{out}{}^{z} + I_{int}{}^{z} \, tanh^2(\kappa.L_{pixel}) = I_{out}{}^{z} + R^z I_0(1 - tanh^2(\kappa.L_{pixel}))^z \times tanh^2(\kappa.L_{pixel}) \tag{6}$$

By summing this previous equation over all the roundtrips, we obtain:

$$\sum_{z=0}^{\infty}(I_{out}{}^{z+1} - I_{out}{}^{z}) = \sum_{z=0}^{\infty}(R(1 - tanh^2(\kappa.L_{pixel})))^z \times I_0 \times tanh^2(\kappa.L_{pixel}) \tag{7}$$

This expression can be simplified using a geometric-progression sum on the right side of the previous equation within which we end up with the following relationship:

$$I_{out}{}^{\infty} = I_0 \frac{tanh^2(\kappa.L_{pixel})}{1 - R(1 - tanh^2(\kappa.L_{pixel}))} \tag{8}$$

The final light extraction efficiency can then be expressed as a function of the lateral extent of the PhC, the grating strength and the reflectance of the lateral mirrors:

$$LEE = \frac{I_{out}{}^{\infty}}{I_0} = \frac{tanh^2(\kappa.L_{pixel})}{1 - R(1 - tanh^2(\kappa.L_{pixel}))} \tag{9}$$

As we can notice, for devices with high lateral extent ($L_{pixel} \gg L_{ext}$ and then $\kappa L_{pixel} \to +\infty$), $tanh^2(\kappa.L_{pixel})$ reaches values close to unity and the denominator becomes quasi-independent on R. Therefore, the light extraction reaches its highest values, which matches the experimental results in Fig. 13 a). For pixels with short lateral sizes ($L_{pixel} < L_{ext}$), the denominator is reflectance-dependent and less than unity. Thus, for given reflectance R and grating strength, LEE decreases with decreasing pixel sizes which supports the validity of this four-wave model to have a better understanding of our experimental results in Fig. 13.

Let us now try to understand how LEE is impacted by the reflectance values for a given device. The coupling strengths of our devices can be deduced from the extraction lengths (e.g., for L_{ext} of ~3 μm, we obtain κ~1/[3 μm]). Using Eq. (9), we evaluate LEE as a function of the lateral extent for different reflectance values (R).

As we can observe in Fig. 15 a), when saturation is not reached yet (pixel with short lateral sizes), increasing the reflectance of the lateral mirrors directly improves LEE at a given lateral extent, which tends to be more significant for reflectance values over ~50 %. In Fig. 15 b), we focus on three particular lateral extents close to those of the short-lateral-size pixels we measured in Fig. 13 (2 μm, 3 μm and 4 μm). We then plotted LEE enhancement factors of pixelated devices over unpixelated ones as a function of the reflectance values. As we can see, the reflectance values have a significant impact on the efficiency of the BMR principle. For instance for pixels with a lateral extent of 2 μm, LEE enhancement over unpixelated devices is close to 1 for low reflectance values (meaning that BMR doesn't have any impact on LEE), reaches ~1.5 for reflectance around 50 %, before going over ~2.5 for high-reflecting mirrors. We measured the reflectance values of our lateral mirrors (Ti5nm-Cu150 nm) and obtained ~50 %, which shows that the potential of BMR within our fabricated devices is drastically hindered by losses in the lateral mirrors. Those low reflectance values were found to be the result of

[5] A half roundtrip also includes reflection by one lateral mirror.

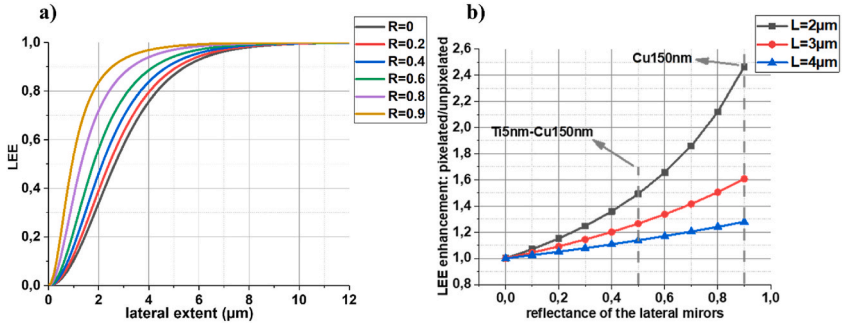

Fig. 15. Simulation results using the herein-developed four-wave model. a) LEE as a function of the PhC lateral extent for different values of the lateral-mirror reflectance. b) ratios between LEE enhancement factors of pixelated (R > 0) and unpixelated (R = 0) devices to evaluate the improvement factors due to BMR.

absorption losses within the thin Ti layer, used for optimal adhesion of Cu on the SiN layer. Additional reflectance measurements performed on bare Ti and Cu layers showed us that reflectance values of Ti mirrors are around 50 %, while Cu itself reaches reflectance values over 90 %. By eliminating this thin Ti layer one could hence expect LEE values in Fig. 13 a) to be even higher for 2 μm pixels and below, as evidenced by the herein-developed model.

4.3. Overall efficiency limitation due to internal quantum decrease

Let us recall that the experimental LEE enhancement values are underestimation of the actual values since they embed IQE decrease due to pixelization. Therefore, the size-dependency of the IQE needs to be further investigated for MQW color converters.

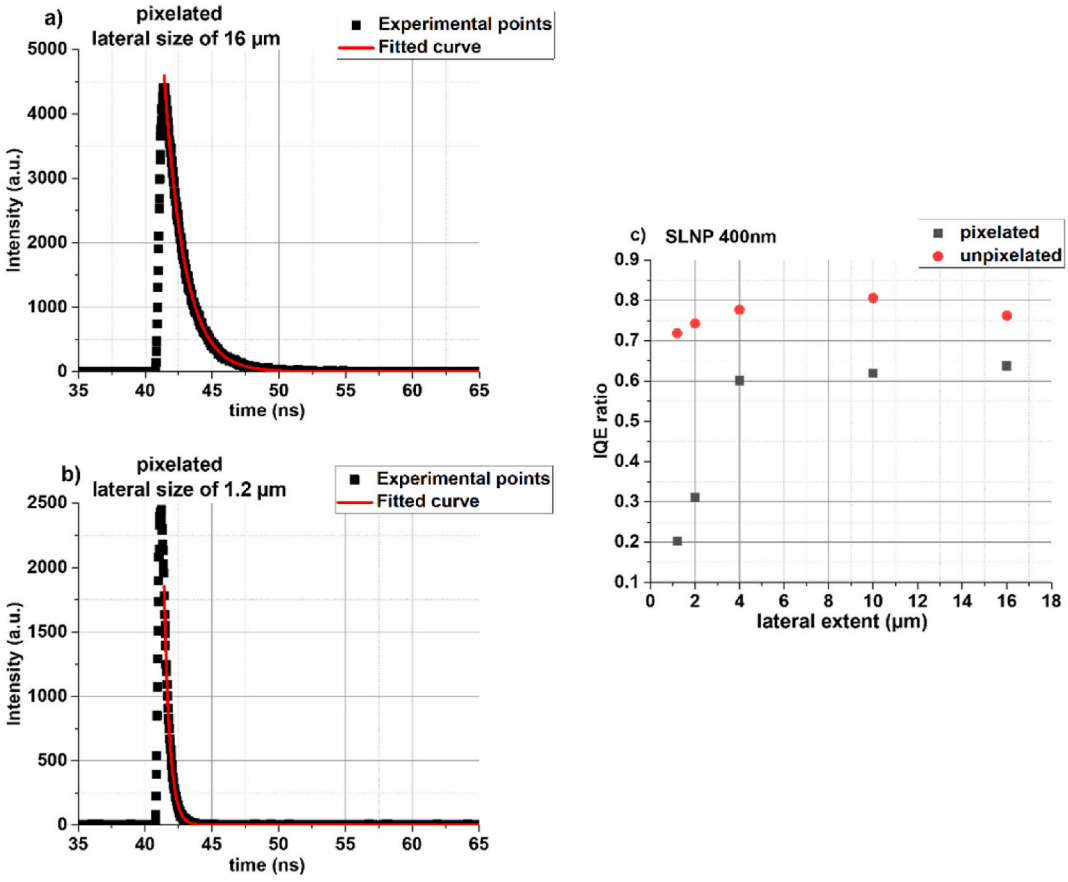

Fig. 16. IQE ratio estimated by TRPL for pixelated and unpixelated patterned CCL with respect to unpatterned and unpixelated references. a-b) transient curves for pixelated structures with lateral extents of 1.2 μm and 16 μm. c) IQE ratio as a function of the lateral extent.

We do so by conducting time-resolved PL measurements (TRPL) to estimate the decay lifetime of the pixelated and unpixelated (but patterned with PhC) devices compared to the reference structures (unpixelated and unpatterned devices). The measurements were conducted using a picosecond laser diode head with a wavelength of excitation of 376 nm, a FWHM of 50 ps with a repetition rate of 5 MHz for pulsed operation. TRPL signals were collected using a solid-state photon counting detector that counts photons emitted at the peak wavelength ~640 nm.

The IQE is given by the ratio of probabilities of radiative ($1/\tau_R$) and total recombination ($1/\tau = 1/\tau_R + 1/\tau_{NR}$), where τ_R and τ_{NR} are the radiative and non-radiative recombination lifetimes [11]. Since the radiative lifetimes do not vary much as explained in Ref. [1], the ratios of the total lifetimes for devices and reference structures directly give the IQE ratios between those two.

The results are displayed in Fig. 16 c) along with transient curves in Fig. 16 a) and 16 b), which were best fit with a single exponential decay function [10]. For the unpixelated (but patterned with PhC) devices, IQE ratios are only slightly size-dependent, with an overall decrease (for all sizes) of ~20 % stemming from the photonic-crystal patterns as explained in Ref. [1]. For pixelated devices on the other hand, IQE ratios rapidly decrease when pixel lateral sizes reach values under 4 μm because of non-radiative recombinations at the pixel's sidewalls. This limit of 4 μm in terms of pixel lateral sizes matches the standard values of carrier diffusion lengths reported for AlGaInP-based devices [12]. We can recall that these phenomena are more detrimental in AlGaInP-based devices than for example in GaN-based devices, because the former have a larger number of surface defect states at their sidewall combined with higher carrier diffusion lengths as well as higher recombination velocities [10]. This is thus the reason why the potential of BMR is also hindered for pixel lateral sizes under 2 μm as seen for SLNP with a = 400 nm and a lateral size of ~1 μm (see Fig. 13). Further extensive experiments that are out of the scope of this article would be required to tackle this issue. In that regard, we can conclude that for now, unless efficient passivation techniques are developed, pixel sizes need to be kept at least over 2 μm. In that framework, this quasi-3D light harnessing strategy could help reach LEE over 40 % and achieve the high luminance required by AR microdisplays with MQW color converters. It is also worth noting that the difference between the saturation values of unpixelated and pixelated devices can be attributed to differences of etch depths wafer-to-wafer due to the technological variations during fabrication.

5. Conclusion

In this study, we have presented the design, fabrication, and characterization of PhC-based InGaP/AlGaInP red MQW color converters that demonstrate outstanding performances in terms of light extraction, pixel sizes, emission directionality, and technological feasibility. By employing a quasi-3D light harnessing principle, which mimics the electromagnetic environment of the final RGB microdisplay, we have achieved promising results. Our fabricated MQW CCL on metallized silicon substrates exhibits highly desirable characteristics, including light extraction efficiencies above 40 % (with pixel lateral sizes over ~2 μm) and directional emission patterns. The process flow has been thoroughly described, offering a pathway for the integration of these devices onto blue μ-LED arrays. Through TRPL measurements and a newly developed four-wave intensity model, we have identified potential areas for further improvement, such as enhancing the reflectance values of back- and lateral-mirrors and developing efficient passivation techniques, especially for pixel lateral sizes under 2 μm. The guidelines established in this work have the potential to revolutionize the next generation of very bright, high-resolution RGB microdisplays for applications in AR glasses and beyond. Our current and future efforts are focused on implementing the fabricated color converters onto blue micro-LED arrays, which will pave the way for significant advancements in this field.

Credit author statement

Amade Ndiaye: Conceptualization, Methodology, Validation, Formal analysis, Investigation, Visualization, Software, Writing – original draft, Writing – review & editing, Ahlem Ghazouani: Investigation, Romain Sommer: Investigation, Elisa Vermande: Investigation, Christine Di Nardo: Investigation, Christian Seassal: Methodology, Formal analysis, Validation Emmanuel Drouard: Methodology, Formal analysis, Validation Christophe Jany: Investigation, Badhise Ben Bakir: Supervision, Conceptualization, Methodology, Validation, Formal analysis, Investigation, Writing – review & editing.

Declaration of competing interest

The authors declare that they have no known competing financial interests or personal relationships that could have appeared to influence the work reported in this paper.

Data availability

Data will be made available on request.

Acknowledgments

The authors would like to thank Manon Arch, Olivier Haon and all the LETI display-integration group for valuable discussions and help on the device fabrication. We also thank Christophe Licitra for his help on the device characterization.

References

[1] A. Ndiaye, A. Ghazouani, C. Seassal, E. Drouard, N. Olivier, B.B. Bakir, Enhanced light-extraction efficiency and emission directivity in compact photonic-crystal based AlGaInP thin-films for color conversion applications, Opt Express, OE 29 (2021) 35965–35979, https://doi.org/10.1364/OE.441116.

[2] E. Quesnel, A. Suhm, M. Consonni, M. Reymermier, G. Lorin, C. Laugier, et al., Experimental and theoretical investigation of 2D nanoplatelet-based conversion layers for color LED microdisplays, Opt Express, OE 29 (2021) 20498–20513, https://doi.org/10.1364/OE.425907.

[3] A. Ndiaye, H.S. Nguyen, A. Ghazouani, C. Seassal, E. Drouard, N. Olivier, et al., Enhanced conversion efficiency and tailored radiation patterns assisted by photonic-crystal light-extractors in compact MQW based color-converters for μLED applications, Light-Emitting Devices, Materials, and Applications XXVI 12022 (2022) 167–175, https://doi.org/10.1117/12.2608502. SPIE.

[4] A. Ndiaye, H.S. Nguyen, C. Seassal, E. Drouard, B. Ben Bakir, Farfield pattern and guided-mode extraction analysis for highly directional emission from photonic-crystal based AlGaInP/InGaP MQW color-converters in thin-film geometry, AIP Adv. 12 (2022), 045122, https://doi.org/10.1063/5.0085930.

[5] J.J. Wierer, A. David, M.M. Megens, III-nitride photonic-crystal light-emitting diodes with high extraction efficiency, Nature Photon 3 (2009) 163–169, https://doi.org/10.1038/nphoton.2009.21.

[6] A. David, T. Fujii, B. Moran, S. Nakamura, S.P. DenBaars, C. Weisbuch, et al., Photonic crystal laser lift-off GaN light-emitting diodes, Appl. Phys. Lett. 88 (2006), 133514, https://doi.org/10.1063/1.2189159.

[7] A. Ndiaye, C. Seassal, E. Drouard, B.B. Bakir, Generalized transfer matrix model for dipole radiation-dynamics modification in layered media: application to incoherent light-emitting structures in thin film geometry, Opt Continuum, OPTCON 2 (2023) 31–53, https://doi.org/10.1364/OPTCON.468231.

[8] W.Y. Fu, H.W. Choi, Development of chipscale InGaN RGB displays using strain-relaxed nanosphere-defined nanopillars, Nanotechnology 33 (2022), 285202, https://doi.org/10.1088/1361-6528/ac6399.

[9] B.O. Jung, W. Lee, J. Kim, M. Choi, H.-Y. Shin, M. Joo, et al., Enhancement in external quantum efficiency of AlGaInP red μ-LED using chemical solution treatment process, Sci. Rep. 11 (2021) 4535, https://doi.org/10.1038/s41598-021-83933-3.

[10] Y. Boussadi, N. Rochat, J.-P. Barnes, B.B. Bakir, P. Ferrandis, B. Masenelli, et al., Investigation of sidewall damage induced by reactive ion etching on AlGaInP MESA for micro-LED application, J. Lumin. 234 (2021), 117937, https://doi.org/10.1016/j.jlumin.2021.117937.

[11] E.F. Schubert, Light-Emitting Diodes, second ed., Cambridge University Press, Cambridge ; New York, 2006.

[12] J.-T. Oh, S.-Y. Lee, Y.-T. Moon, J.H. Moon, S. Park, K.Y. Hong, et al., Light output performance of red AlGaInP-based light emitting diodes with different chip geometries and structures, Opt Express, OE 26 (2018) 11194–11200, https://doi.org/10.1364/OE.26.011194.